Miocene bimodal magmatism in the Packsaddle Volcanic Complex, Fuegian Andes, southernmost South America: evidence of oceanic-ridge subduction

Cristóbal Ramírez de Arellano[a,*]; Mauricio Calderón[b]; Benjamín Aspillaga[a]; Gonzalo Galaz[c]; Pierre Yves Descote[a]; Israel Donoso[a]; C. Mark Fanning[d]; Marly Babinski[e]; Fernando Poblete[f]

a: Earth Science School, Universidad Andrés Bello, Santiago, Chile. República 220, Santiago, Chile.

b: Facultad de Ingeniería, Universidad del Desarrollo. Avenida Plaza 680, Las Condes, Santiago, Chile.

c: Departamento de Geología, Universidad de Atacama. Av. Copayapu 358, Copiapó, Chile.

d: Research School of Earth Sciences, Australian National University. 142 Mills Rd, Acton ACT 0200, Canberra, Australia.

e: Instituto de Geociências, Universidade de São Paulo. R. do Lago, 562 - Butantã, São Paulo, Brasil.

f: Departamento de Geología, Universidad de Chile. Plaza Ercilla 803, Santiago, Chile.

Emails:

cristobal.ramirez@unab.cl

mauriciocalderon@udd.cl

b.aspillagaortega@uandresbello.edu

ggalaz@gmail.com

pierre.descote@unab.cl

i.donosoarenas@gmail.com

cmarkfanning@gmail.com

babinski@usp.br

ferpoble@uchile.cl

Abstract

Oceanic ridge subduction is known to generate anomalous magmatism before and during the opening of the slab window. High Sr/Y intermediate magmas and slightly alkaline basalts with transitional arc-to-intraplate (OIB-like) signatures have been reported worldwide in such tectonic settings. Southernmost South America has been affected by the subduction of several spreading ridges from the late Oligocene to the present. Here we present new geochronological, petrographic, geochemical, and isotopic data to evaluate the petrogenesis of two Lower Miocene volcanic units from the Fuegian archipelago at ~56° S, formed during subduction of the Nazca-Phoenix spreading ridge. Comparison with igneous suites related to subduction of the Chile Ridge (currently being subducted beneath central Patagonia at ~46.5° S) reveals notable similarities in timing relative to slab-window formation and in chemical signatures. We interpret the high Sr/Y chemistry as resulting from amphibole fractionation and delayed plagioclase crystallization at depth from calc-alkaline melts, with input of terrigenous material via mantle contamination or lower-crust assimilation. The slightly alkaline magmas reflect lower degrees of partial melting due to a different thermal structure of the slab-mantle wedge.

Keywords: ridge subduction, slab-window, alkaline magmatism, high Sr/Y, Patagonia

Magmatismo bimodal mioceno en el Complejo Volcánico Packsaddle, Andes Fueguinos, extremo sur de América del Sur: evidencias de subducción de dorsales oceánicas. La subducción de dorsales oceánicas genera magmatismo anómalo antes y durante la apertura de la ventana astenosférica. En distintas partes del mundo, con este contexto tectónico, se han registrado magmas intermedios de alto Sr/Y y basálticos ligeramente alcalinos con rasgos transicionales entre arco e intraplaca (tipo OIB). El extremo sur de América del Sur ha sido afectado por la subducción de varias dorsales desde

el Oligoceno tardío hasta el presente. Aquí presentamos nuevos datos geocronológicos, petrográficos, geoquímicos e isotópicos para evaluar la petrogénesis de dos unidades volcánicas del Mioceno Inferior del Archipiélago Fueguino (~56° S), formadas durante la subducción de la dorsal Nazca-Phoenix. La comparación con series ígneas relacionadas con la subducción de la Dorsal de Chile (actualmente en subducción bajo la Patagonia central, ~46.5° S) revela notables similitudes en su temporalidad respecto a la formación de la ventana astenosférica y en sus firmas químicas. Interpretamos la química de alto Sr/Y como el resultado de fraccionamiento de anfíbola y de la cristalización tardía de plagioclasa en profundidad, a partir de magmas calco-alcalinos, con aporte de material terrígeno vía contaminación del manto o asimilación de la corteza inferior. Los magmas ligeramente alcalinos reflejan menores grados de fusión parcial debido a una estructura térmica de la cuña mantélica distinta.

Palabras clave: subducción de dorsales, ventana astenosférica, magmatismo alcalino, alto Sr/Y, Patagonia.

Introduction

The chemistry of igneous rocks from subduction settings typically follows a calc-alkaline differentiation trend originating from basaltic primary melts (Wilson, 1989). Nevertheless, a variety of subduction-related primary magmas belonging to different magma series have been described (Schmidt and Jagoutz, 2017). In tectonic settings where oceanic spreading ridges are subducted, two distinct series often coexist: slightly alkaline transitional magmas derived from low-silica basaltic primary melts, and magmas produced by andesitic primary melts, often with high Sr/Y ratios and following a subalkaline trend (Yogodzinski et al., 2001; Gómez-Tuena et al., 2018; Ramírez-de-Arellano et al., 2021; Zhen et al., 2025).

Southern South America has been influenced by the subduction of several spreading ridges from the late Oligocene to the present. Miocene volcanic and plutonic rocks with transitional (slightly alkaline) composition have been reported between 47° and 50° S (Ramos and Kay, 1992; Gorring et al., 1997; D'Orazio et al., 2004; Guivel et al., 2006; Corbella and Lara, 2008). These rocks are roughly coeval with high Sr/Y andesites (Kay et al., 1993; Ramos et al., 2004; Orihashi et al., 2013). With ages from 12 Ma to present, they predate the opening of the slab window associated with the subduction of the Chile Ridge (Kay et al., 1993; Ramírez-de-Arellano et al., 2012, 2021). Similarly, in southernmost South America, at the latitude of Tierra del Fuego (55° S), Miocene basaltic and andesitic rocks showing both compositional types have been reported on the continental margin of the Scotia Plate. They have been grouped as the Packsaddle Volcanic Complex (PVC) exposed on different islands of the Fuegian archipelago (Suárez et al., 1985; Fig. 1). Available geochemical data are however limited, and ages are poorly constrained to ca. 18–21 Ma (K-Ar dating; Puig et al., 1984). Regional palaeogeographic reconstruction indicates that the Nazca-Phoenix spreading ridge has been located off Tierra del Fuego since ca. 30 Ma (Eagles and Jokat, 2014), implying a spatial and temporal relation between the Nazca-Phoenix Ridge and the PVC.

Given these Patagonian occurrences linked to the subduction of two different spreading-ridges, it remains unclear whether the two magma types formed simultaneously or reflect a magmatic transition. It is also unclear which common conditions favor their genesis. Here, we provide new data on field relations of volcanic and volcaniclastic units, petrography, geochemistry and geochronology of the PVC to evaluate its petrogenesis and the causal relationship of transitional (slightly alkaline) and the high Sr/Y andesitic magmatism to spreading-ridge subduction.

Tectonic and geologic setting

The subduction of several oceanic spreading ridges occurred along the southernmost segment of South America from the Palaeogene to the Neogene (Fig. 2). The Farallon-Phoenix Ridge migrated southward relative to South America from the Mesozoic and reached the Tierra del Fuego region (~53° S) by the Oligocene Epoch, at ca. 30 Ma (Pardo-Casas and Molnar, 1987; Eagles and Jokat, 2014; Eagles and Scott, 2014). Following the breakup of the Farallon Plate and a major plate reorganization in the late Oligocene (ca. 26 Ma), the Farallon-Phoenix Ridge became known as the Nazca-Phoenix Ridge (NAZ-PHO) and continued to be subducted beneath Tierra del Fuego until ca. 20 Ma (e.g., Eagles and Jokat, 2014; Eagles and Scott, 2014). Migration concluded with the subduction of the triple junction between the Nazca, Phoenix, and Antarctic plates, after which two separate ridges were subducted (Eagles and Jokat, 2014; Eagles and Scott, 2014; see figure 2). The Nazca-Antarctica Ridge migrated rapidly northward to its present position near the Taitao Peninsula (~46.5° S) and is now referred to as the Chile Ridge (Cande and Leslie, 1986; Pardo-Casas and Molnar, 1987; Breitsprecher and Thorkelson, 2009). It is proposed that the Antarctic-Phoenix Ridge (ANT-PHO) migrated southward, from ~54° to 57.5° S along the southwestern margin of the Scotia Plate (Eagles and Jokat, 2014; Eagles and Scott, 2014; see figure 2). The separate subduction of the Chile Ridge and the ANT-PHO Ridge produced distinct structural and magmatic effects in their respective segments of the margin. Ramírez-de-Arellano et al. (2021) proposed the terms Patagonian and Fuegian domains, separated by the South America-Scotia plate boundary at ~53° S, to describe the contrasting chemical signatures in these two Andean segments.

In the Patagonian domain (north of 53° S), Chile Ridge subduction at ca. 16 Ma is invoked to explain rapid exhumation and development of the Magallanes Fold-and-Thrust Belt (Ramos, 2005; Stevens-Goddard and Fosdick, 2019; Muller et al., 2024). In this segment, the exhumation exposes Lower

Miocene calc-alkaline plutonic rocks (Hervé et al., 2007), where they crop out in ranges reaching up to ~3,000 m a.s.l. (Nullo et al., 1978; Ramos, 2005; Ramírez-de-Arellano et al., 2012). Plutonic rocks from the batholith and satellite plutons record progressive eastward arc migration during the Early Miocene (Espinoza et al., 2010; Ramírez-de-Arellano et al., 2012). During the Late Miocene, after 12 Ma, the eastern Andes of Patagonia experienced 'transitional' magmatism, becoming increasingly enriched in alkalis compared to the typical calc-alkaline products of the batholith (e.g. Gorring et al., 1997; D'Orazio et al., 2004; Guivel et al., 2006; Corbella and Lara, 2008). Coeval (14 to 11 Ma) volcanic and subvolcanic andesites with high Sr/Y ratios (>20) have been reported along this arc domain as well (Kay et al., 1993; Ramos et al., 2004).

In the Fuegian domain (that is, south of 53° S), Lower Miocene sedimentary and volcanic rocks are still preserved, implying lower exhumation rates with respect to the Patagonian domain. Suárez et al. (1985) described two Miocene (Burdigalian) volcanic units enclosed within the Packsaddle Volcanic Complex (PVC). The sparse chemistry of these rocks suggests that these two units could resemble the alkaline-transitional and the high Sr/Y rocks from the Patagonian domain (Puig et al., 1984; Ramírez-de-Arellano et al., 2021).

The PVC was studied by Hervé et al. (1984), Puig et al. (1984), and Suárez et al. (1985), in the context of a regional (1:250,000 scale) geological study (Fig. 1A). The PVC unconformably overlies deformed Upper Jurassic to Lower Cretaceous igneous rocks and deformed sedimentary rocks related to the Rocas Verdes marginal basin (Dalziel et al., 1974; Suárez et al., 1985; Stern and de Witt, 2003; Calderón et al., 2007). At some places, the PVC also overlies Palaeogene plutonic rocks from the Seno de Año Nuevo Group of Suárez et al. (1985), who described two units of andesites and alkaline basalts. A PVC andesite was dated at 21.4±0.2 Ma by K-Ar in whole-rock (average of 21.4±0.2 and 21.4±0.4 Ma; Puig et al., 1984; see figure 1A). These rocks crop out on Hardy Peninsula (Fig. 1A) as

isolated bodies and were described as porphyritic andesites and volcanic breccias (Suárez et al., 1985). Alkaline basalts cropping out on Packsaddle Island were dated by K-Ar in whole-rock at 18.5±0.2 Ma (average of 18.2±1.3, 18.5±0.2, and 18.8±1.2 Ma; Puig et al., 1984; see figure 1A), indicating that they probably postdate the andesitic rocks, although the contact relationship between these two volcanic units was not reported.

In more recent fieldwork conducted by the authors, volcanic and volcaniclastic rocks of the PVC were studied at three localities: Packsaddle Island, Pacha Island, and Hardy Peninsula on Hoste Island (Fig. 1A). In a broad sense, the representative lithologies are olivine-bearing basalts on Packsaddle Island and hornblende-bearing dacites on Pacha Island (Fig. 1B, C).

The outcrops at Packsaddle Island are mainly composed of a 30 m-thick basalt layer, well exposed along the southern side of the island, with a characteristic colonnade structure (Fig. 3A). Previous studies interpreted this body as a lava flow, yet without providing a detailed description of its contacts with adjacent rocks. In our study, newly identified field relationships suggest that it may instead correspond to a hypabyssal intrusion, likely a sill, emplaced within a succession of volcanic and volcaniclastic rocks. The lower contact of the basaltic unit is sharp and markedly irregular, truncating the underlying volcanic breccia with a sharp cross-cutting relationship (Fig. 3B). The breccia layers have a minimum thickness of 20 m (Fig. 3C). They are characterized by a pyroclastic matrix that comprises up to 70 vol.% of the rock (60–80% lapilli and 20–40% ash) and contain andesitic-dacitic clasts and subordinate crystalline tuff fragments ranging from a few cm to blocks over two m in diameter. Abundant clasts of hornblende-bearing dacite, like those from Pacha Island, are found in these breccias. The volcanic rocks from Packsaddle Island are overlain by an unconsolidated (Holocene?), fine-grained and matrix-supported marine-lacustrine deposit (Fig. 1B). This deposit contains subrounded polymictic clasts (<5 mm size) and marine fossils, such as bivalves.

On Hardy Peninsula (Fig. 1A, B), lava flows, breccias and subvolcanic dikes alternate with gabbros and diorites of satellite intrusions of the Fuegian Batholith. Volcanic rocks from the PVC could easily be confused with the Jurassic rocks from the Hardy Formation, which consist of intermediate to felsic lavas and breccias.

The Pacha Island (Fig. 1C), located ~30 km north of Packsaddle Island, is mainly composed of hornblende-bearing dacitic lavas, with a characteristic entablature structure, overlying deformed rocks of the Yaghan Formation and isolated monzonitic plutons of the Fuegian Batholith. Small outcrops (<10 m^2) of tuff can be observed at the base of the lavas.

Following Suárez et al. (1985) and the recommendations of Ricci et al. (1993), we propose the name 'Packsaddle Basalts' for the olivine basalts and volcaniclastic breccias of Packsaddle Island and the isolated outcrops on Hardy Peninsula, and 'Pacha Dacites' for the hornblende-bearing andesites and dacites of Pacha Island and Hardy Peninsula. Both units are part of the PVC. Schematic stratigraphic columns with sample locations are shown in figure 1.

Methods

Forty samples from the PVC, including samples from the Packsaddle and Pacha islands and the surrounding areas, were petrographically analysed under a Nikon Eclipse E200 polarizing microscope to identify the texture and modal mineralogy of volcanic (lavas, tuff and breccias) and subvolcanic rocks.

New whole-rock geochemical data from nine samples of the PVC are presented in Table 1. They include two clasts of hornblende-biotite dacite of the lower breccia from Packsaddle Island, an olivine basalt from the same island, two dacites from Pacha Island, and four samples from Hardy

Peninsula (two plutonic, a micro-gabbro and an olivine basalt). These samples were analysed for major and trace element compositions using ICP-AES (inductively coupled plasma atomic emission spectroscopy) and ICP-MS (inductively coupled plasma mass spectroscopy) at Activation Laboratories Ltd. (Actlabs) in Vancouver, Canada. Different element ratios were used to classify the volcanic units and evaluate petrogenetic processes (see below).

A new U-Pb zircon age was obtained for a clast of hornblende-biotite dacite of the Pacha Dacite unit, from the volcanic breccia at Packsaddle Island (sample FC2362-A), using SHRIMP II (sensitive high-resolution ion microprobe) at the Research School of Earth Sciences, Australian National University, in Canberra, Australia. Analytical techniques essentially follow those given in Williams (1998), comprising six scans through the mass spectrum, with the Temora 1 reference zircon (Black et al., 2003) used to calibrate the U/Pb ratios. The data were processed using the SQUID add-in Excel Macro of Ludwig (2000) and corrections for common Pb made using the measured $^{238}U/^{206}Pb$ and $^{207}Pb/^{206}Pb$ ratios following Tera and Wasserburg (1972) as outlined in Williams (1998). Results are shown in Table 2. Uncertainties in weighted mean age calculations are reported at the 2σ level. The geological time scale used follows the Chronostratigraphic Chart 2022 by IUGS-ICS.

Sr and Nd isotope determinations of a dacite breccia clast and an olivine basalt from Packsaddle Island, one micro-gabbro from Hardy Peninsula, and one dacite from Pacha Island were carried out at the Geochronological Research Centre at Universidade de São Paulo, Brazil (Table 3). Rock powders (100 mg) were dissolved in Savillex beakers with HF and HNO_3 on a hot plate for 5 days at 110 °C, dried down on a hot plate, and the residue was dissolved in 6 M HCl at 110 °C for 24 hours. The HCl solution was dried down and converted to nitrates with concentrated HNO_3. Sr was separated using Eichrom Sr-Spec® resin and eluted with 0.05 M HNO_3. Nd was purified using two

steps of ion-exchange columns with RE-Spec® and LN-Spec® resins; Nd was eluted in 0.26 M HCl. The Sr isotope ratios were determined on a Triton TIMS (thermo-ionization mass spectrometer) in dynamic mode. The ratios were normalized to $^{86}Sr/^{88}Sr=0.1194$, and the NBS987 standard analysed during this study gave a mean $^{87}Sr/^{86}Sr$ value of 0.710250±0.000018 (2σ). The Sr blanks were about 128 pg. The Nd isotope ratios were determined on a Thermo Scientific Neptune multicollector ICP-MS. The ratios were normalized to $^{146}Nd/^{144}Nd=0.7219$, and the $^{143}Nd/^{144}Nd$ average for the JNdi-1 standard analysed during this study was 0.512197±0.000004 (2σ). The analytical blanks were about 270 pg.

Results

Petrography of the PVC

The olivine basalts from Packsaddle Island constitute the uppermost, larger, unit of the island. They exhibit a pilotaxitic texture, with olivine and plagioclase phenocrysts (Fig. 4A). The groundmass occupies ~90% of the rock volume and consists primarily of plagioclase (65%), minor pyroxene and olivine microliths (5%), and glass (30%).

The lower stratigraphic unit observed at Packsaddle is of pyroxene basalts located in the east of the island. These basalts comprise cumulates of clinopyroxenes and minor olivine in a microcrystalline groundmass mainly composed of plagioclase microliths, clinopyroxene, and glass. Breccias overlying the lower basalts show variation in the size and nature of their clasts, but all have a vitreous-crystalline matrix with abundant clasts of porphyritic hornblende-bearing andesites and dacites (Fig. 4B). The dated crystalline tuff (FC2362-A) presents abundant crystals (~30%, <1mm), mainly plagioclase, hornblende, and minor biotite in a vitreous-crystalline matrix.

228 The two dacite samples (66 wt.% SiO_2) from Pacha Island exhibit a porphyritic texture, with 75–85%
229 groundmass, predominantly pilotaxitic, consisting of plagioclase microliths, along with granular
230 quartz, and minor volcanic glass and oxides (Fig. 4C). Phenocrysts are primarily hornblende and
231 plagioclase (3:1). Hornblende is subhedral (0.3–1.5 mm), in some cases poikilitic, enclosing
232 plagioclase crystals. Conversely, euhedral to subhedral plagioclase phenocrysts (0.3 to 1.0 mm) show
233 Carlsbad twinning and subtle compositional zoning. Sieve textures and reabsorbed rims are
234 common.

235

236 ***Geochemistry of the PVC***

237 New geochemical data are reported from nine samples of basalts, andesites, dacites and intrusive
238 from Packsaddle Island, Pacha Island, and Hardy Peninsula (Figs. 5 and 6; Table 1). The results are
239 combined with previously published data from the PVC (Puig et al., 1984; Ramírez-de-Arellano et al.,
240 2021) and the integrated datasets are compared with data for three Neogene igneous suites from
241 the Patagonia domain to the north of the studied area, as defined by Ramírez-de-Arellano et al.
242 (2021).

243 The olivine basalts from Packsaddle Island show alkaline to subalkaline affinities (Fig. 5A) in a narrow
244 range of SiO_2 (47.2–49.5 wt.%), with high Mg# (~66.5%), Ni ~ 160 ppm (up to 220 ppm), Cr ~ 320
245 ppm (up to 380 ppm), and high concentration of TiO_2 and P_2O_5 (>1.5 wt.% and >0.3 wt.%,
246 respectively). Three samples reported by Puig et al. (1984) and two samples reported by Ramírez-
247 de-Arellano et al. (2021) follow the same trends. In a multi-element diagram normalized to Primitive
248 Mantle (Fig. 6) these rocks show an enrichment of large ion lithophile elements (LILE). However, the
249 preferential enrichment of LILE over high field strength elements (HFSE), typical of arc magmas, is
250 not pronounced, as also indicated by the low Ba/Nb ratios (<30, except one at 47; Fig. 5F). These

rocks show positive anomalies of Ti and P compared to heavy rare earth elements (HREE) like Gd or Tb (Fig. 6). Only a subtle Pb positive anomaly is observed (Ce/Pb >3; Fig. 6). In terms of REE, these rocks also present a preferential enrichment of light rare earth elements (LREE) over HREE, with no Eu anomaly (Fig. 6). The $(La/Yb)_n$ and $(Dy/Yb)_n$ ratios are moderately high (~9 and ~1.3, respectively), exhibiting a narrow variability. In comparison with common arc-related magmas (e.g., South Patagonian Batholith and Southern Volcanic Zone of the Andes; Hervé et al., 2007; Hickey-Vargas et al. 2016), these rocks have low Rb/Ba, Ba/Nb (<0.04 and <30, respectively; Fig. 5D, F), and high Nb/U (>13.7), Sr/Y (>38; Fig. 5C), Ce/Pb (>3) and La/Th (>6.4; Fig. 5E) ratios. These element ratios indicate a signature intermediate between arc and intraplate (OIB-like).

The dacites from Pacha Island share a common signature with the dacite clasts from the pyroclastic breccias at Packsaddle Island and the andesites and dacites from Hardy Peninsula reported by Puig et al. (1984). As shown in figure 5A, these rocks display a subalkaline character, well below the line separating alkaline from subalkaline fields, covering a compositional range of 61 to 65 wt.% SiO_2, 18.2 to 16.5 wt.% Al_2O_3, TiO_2 <0.85 wt.%, P_2O_5 <0.25 wt.%, and relatively high Mg# (e.g., 57 at 57.3 wt.% SiO_2; 44 at 63 wt.% SiO_2). Notably, these rocks exhibit low K/Na ratios (<0.5) comparable to the Archean TTG suites (Fig. 5B). There is a clear arc-like trace element signature, namely a preferential enrichment of LILE over HFSE with a marked Nb-Ta negative anomaly, high Rb/Ba ratios (>0.05), and a well-marked Pb positive anomaly (Ce/Pb <2.2), as shown in the multi-element diagram normalized to Primitive Mantle (Fig. 6). In terms of the REE, these rocks are preferentially enriched in LREE over HREE, with a relatively high $(La/Yb)_n$ and moderated $(Dy/Yb)_n$ ratios (~11 and ~1.2, respectively), like the olivine basalts from Packsaddle Island, and a notable absence of Eu anomalies (Fig. 6). As mentioned, the most remarkable feature of these rocks is their high Sr/Y ratios (>40; Fig. 5C), due to their relatively high Sr contents (>570 ppm). Another feature of these rocks is the Th and U higher than K and Rb when normalized to Primitive Mantle (Fig. 6).

The signatures of the micro-gabbro (FC2349) from Hardy Peninsula (51.6 wt.% SiO_2; Mg# 65) and the plutonic rocks from the same locality, differ from those of the Pacha Dacites and Packsaddle Basalts (Fig. 6). They display a subalkaline character and trace element ratios (e.g. Ba/Nb >70; Sr/Y <40) similar to those observed in most of the plutons from the Patagonian Batholith and volcanic products of the Southern Volcanic Zone of the Andes (Hervé et al., 2007; Hickey-Vargas et al., 2016).

U-Pb zircon geochronology

Zircons from a hornblende vitreous-crystalline dacite tuff fragment within the lower volcanic breccia of Packsaddle Island were analysed. The sample (FC2362-A) consists of crystals (30%; < 1mm), mainly plagioclase, hornblende, and minor biotite, in a vitreous to crystalline matrix (70%). The breccia is intruded by a basaltic sill and is thus expected to record the age of explosive andesite-dacite volcanism prior to the emplacement of the basalts. Twenty-two zircons were analysed by SHRIMP U-Pb (Table 2). Twenty-one grains yield a mean age of 20.5±0.2 Ma (Fig. 7). One zircon yielded an age of ca. 104 Ma and is presumed to be an inherited xenocryst.

Isotope chemistry of the PVC

Sr and Nd isotope compositions of five samples were determined (Fig. 8; Table 3): two olivine basalts and the dated dacite tuff clast from Packsaddle Island, a dacite from Pacha Island, and a micro-gabbro from Hardy Peninsula.

The two basalts yield indistinguishable initial $^{87}Sr/^{86}Sr$ (0.70392 and 0.70387) and $^{143}Nd/^{144}Nd$ (0.512870 and 0.512878; εNd_i = +5.0/5.2) ratios. The micro-gabbro (FC2349) from Hardy Peninsula has a radiogenic signature similar to the Packsaddle basalts ($^{87}Sr/^{86}Sr_i$=0.70369; εNd_i=+4.7). The

297 dated tuff clast from the lower breccia on Packsaddle Island shows a similar initial $^{87}Sr/^{86}Sr$ (0.70396)
298 and a lower initial $^{143}Nd/^{144}Nd$ (0.512749, εNd_i=+2.7) compared to the basalts. The Pacha Island
299 dacite has the highest initial $^{87}Sr/^{86}Sr$ (0.70446), but a comparable $^{143}Nd/^{144}Nd_i$=0.512798 (εNd_i=+3.6)
300 to the dated dacitic clast.

301

302 **Discussion**

303 ***Petrogenesis of the Packsaddle Basalts***

304 The low SiO_2 concentration of these rocks (<50 wt.%), together with their high Mg# (up to 67), high
305 concentration of Ni (up to 220 ppm) and Cr (up to 380 ppm), and their uniform Sr and Nd isotope
306 compositions, suggests a mantle source of magmas with little chemical differentiation or crustal
307 assimilation. Their transitional geochemistry between alkaline and subalkaline affinities suggests low
308 degrees of melting, while their high FeO/MgO ratios, at the boundary between tholeiitic and calc-
309 alkaline series, suggest less oxidizing conditions than for the typical calc-alkaline magmas of the
310 Patagonian Batholith and lavas from the Southern Volcanic Zone (Hervé et al., 2007; Hickey-Vargas
311 et al., 2016). Their trace element signatures, with transition from arc-related to intraplate (OIB-like)
312 affinities, suggest important variation either in the mantle source or in the thermodynamic
313 conditions that generated these magmas compared with “Andean” conditions.

314 Upper Miocene (<8 Ma) OIB-like basalts along Patagonian and Antarctic Peninsula margins coincide
315 spatially with the current slab windows associated with the Chile Ridge (Nazca-Antarctica Ridge) and
316 the Antarctic-Phoenix Ridge, respectively (e.g., Gorring and Kay 2001; D‘Orazio et al., 2004; Hole et
317 al., 2021, 2023). Hole et al. (2023) proposed that they were generated from a source dominated by
318 pyroxenites instead of the peridotites of typical arc mantle sources. In this model, the transitional
319 magmas of the Packsaddle Basalts could have been generated from an intermediate source, due to

a shifting of the locus of mantle melting or due to erosion of lithospheric mantle as proposed by Turner et al. (2017). Their LILE patterns (e.g., with Cs and Rb less enriched than Ba and K and low Rb/Ba; see figures 5 and 6) would support a mixture between a subduction-like and an OIB-like sources. Nevertheless, other geochemical features of the Packsaddle Basalts require explanation. The high concentration of REE, consistently with relative enrichment in alkalis, supports lower degrees of melting than for typical calc-alkaline rocks. Likewise, the less oxidizing conditions suggested by the high Feo/MgO ratios would be consistent with the low concentration of fluid-mobile elements such as Pb and U compared to LREE (see figure 6), indicating a lower flux of fluid from the slab. Finally, the high concentration of HFSE, mainly Nb, Ta, and TiO_2, compared to LILE (as shown by the low Ba/Nb ratios; see figures 5 and 6), suggests decreasing stability of refractory phases such as rutile, which is thought to be the main carrier of these elements to the lower mantle. Considering that rutile is stable at pressures higher than ~1.5 GPa and temperatures lower than ~1000 °C (for a system with 2% H_2O; Xiong et al., 2005; Skora and Blundy, 2010), its instability could be related to warmer conditions during slab dehydration (see figure 9) or melting of a lithospheric mantle previously enriched. These conditions could indicate an abnormal thermal regime induced by the presence of the NAZ-PHO slab window immediately to the north of this region. Similar conditions in the context of Chile Ridge subduction allowed melt extraction at intermediate degrees of mantle melting (Ramírez-de-Arellano et al., 2021).

The isotopic composition of Packsaddle Basalts resembles the less contaminated products of the Patagonian Batholith ($^{87}Sr/^{86}Sr_i \approx 0.7038$; $\varepsilon Nd_i \approx 5.0$; Hervé et al., 2007), confirming minimal crustal anataxis and implying rapid ascent (see figure 8). The isotopic difference with respect to a depleted MORB mantle, calculated at 20 Ma ($^{87}Sr/^{86}Sr_i=0.70263$; $^{143}Nd/^{144}Nd_i=0.51313$; Salters and Stracke, 2004) can be attributed to fluid-melt interactions with the mantle wedge or to ancient enriched domains in the lithospheric mantle.

Petrogenesis of the Pacha Dacites

The Pacha Dacites exhibit a clear arc-related trace element signature with a notable enrichment of LILE over HFSE, a negative anomaly of Ti, and a positive anomaly of Pb (see figure 6). However, they also present certain features that distinguish them from typical arc magmas, namely low K/Na ratios, relatively high Mg# (with respect to SiO_2 concentration), relatively high Sr/Y and La/Yb ratios, absence of Eu anomaly, and low HREE concentrations (see figures 5 and 6). The high Sr/Y together with the low K/Na ratios and the absence of Eu anomaly can be attributed to a lack of fractionation or delayed plagioclase crystallization, which is rare for such evolved rock compositions. Experimental and theoretical studies show that dissolved H_2O in the magma, and pressure, significantly influence plagioclase stability and crystallization order in mafic-intermediate systems (e.g., Goldsmith 1982; Gaetani et al., 1993). Given the calc-alkaline character and the abundance of hornblende in the Pacha Dacites, the parent magmas must have had high water contents. It is hard to make a precise estimate of the pressure: high-pressure magma differentiation is characterized by amphibole or garnet, either as a fractionated phase or as a stable phase in the residue (e.g., Davidson et al., 2007; Gao et al., 2023). These two phases have high HREE partition coefficients (K_D>1): amphibole has similar K_D for all HREE from Dy to Yb, whereas garnet has $K_D(Yb)>>K_D(Dy)>1$ (*ibid*.). The high La/Yb ratios observed in the Pacha Dacites could indicate the effect of both minerals. Nevertheless, despite the low concentration of HREE (only two to three times that of Primitive Mantle), the relatively low Dy/Yb ratios (see figure 6) argue in favour of amphibole fractionation. The relatively high Mg# at a given SiO_2 compared to a typical calc-alkaline series may also be explained by amphibole fractionation. Because of its low SiO_2 concentration, fractionation of amphibole would increase SiO_2 in the residual melt more efficiently than clinopyroxene (the other ferromagnesian candidate). The low La/Th ratios (indicative of high Th concentration; see figure 5) observed in the Pacha Dacites,

367 together with the slightly less radiogenic Sr isotopic signature, suggest some participation of crustal
368 material, possibly from sediment subduction, during melting in the mantle wedge (see figure 8).

369 Partial melting of mafic rocks from the slab or the sub-arc crust has been invoked to explain the
370 genesis of high Sr/Y rocks (e.g., Defant and Drummond 1990; Moyen 2009; Yang et al., 2020; Zhang
371 et al., 2021; Wang et al., 2022; Xu and Chen, 2023). Conversely, high-pressure experiments have
372 shown that amphibole fractionation and delayed plagioclase crystallization can also generate high
373 Sr/Y melts (Müntener et al., 2001; Davidson et al., 2007; Alonso-Perez et al., 2009; Nandedkar et al.
374 2014, 2016; Gao et al., 2023). It has also been proposed that the parental magmas for these suites
375 could be mantle-derived high-Mg andesites (HMA) resulting from re-equilibration of basaltic melts
376 in the upper section of the mantle wedge (Schmidt and Jagoutz, 2017).

377 Despite the sparse sampling, the absence of mafic (basaltic) members with the trace-element
378 characteristics of the Pacha Dacites, combined with the relative homogeneity of trace-element ratios
379 for andesites to dacites (60–65 wt.% SiO_2), suggests that their parental melts were intermediate,
380 probably high-Mg andesites. Because there is no evidence for garnet involvement in the evolution
381 of the Pacha Dacites, we favour a deep fractional-crystallization model from an intermediate parent
382 magma, characterized by amphibole fractionation with delayed plagioclase crystallization.
383 Differentiation may have been accompanied by some mid- to lower-crustal assimilation to account
384 for the elevated Th concentrations and isotopic signature of the Pacha Dacites (see figures 5, 6, and
385 8). The interpreted deep fractional-crystallization process means that upper-crustal contamination
386 is unlikely. Mantle-derived contamination, either via metasomatism with subducted sediments or
387 melting of a heterogeneous lithospheric mantle, cannot be ruled out. Testing in detail any of these
388 hypotheses falls outside the scope of this work, and a detailed isotopic study would be required.

389

Time, spatial and geochemical relationship

The available time constraints and the lack of any evidence for a mixing trend between the signatures from Packsaddle Basalts and Pacha Dacites suggest two discrete volcanic events rather than coeval bimodal magmatism or a continuous variation in the melting mechanism: we rather propose intermediate volcanism dominated by high Sr/Y andesites and dacites, later followed by olivine-bearing basaltic magmas. This is consistent with the new U-Pb zircon age (20.5±0.2 Ma) and the previous K-Ar dating of 21±0.2 Ma for a dacite and 18.5±0.2 Ma for the olivine basalts (Puig et al., 1984). The distinctive geochemical characteristics of the Pacha Dacites are also observed in the breccia clast from Packsaddle Island and the andesite-dacites from Hardy Peninsula reported by Suárez et al. (1985). In contrast, the micro-gabbro (FC2349) and associated plutonic rocks from Hardy Peninsula do not match either the Pacha Dacites or the Packsaddle Basalts, and it could correspond to an even earlier magmatic event. No field relationships have been observed among these three units aside from the breccia on Packsaddle Island.

Given the age established, a causal relationship between PVC magmatism and the subduction of the NAZ-PHO spreading ridge is feasible. Tectonic reconstruction shows the correspondence between the location of the PVC and the slab window generated by the NAZ-PHO ridge (Breitsprecher and Thorkelson, 2009; Eagle and Jokat, 2014; Eagles and Scott, 2014) (Fig. 2). Despite the fast motion (>10 km/Myr) of the Nazca and Phoenix plates with respect to the South American plate at 20 Ma, the low relative velocity between these two oceanic plates generated a narrow E-W oriented slab window below the Fuegian domain (Scotia Plate) to the north of the PVC (Fig. 2 left panel; Fig. 9). At that time, the high Sr/Y intermediate magmas were erupted above the slab corresponding to the Phoenix Plate. Between 20 and 16 Ma, subduction of the Nazca-Phoenix-Antarctic triple junction widened the slab window, ultimately leaving the PVC above it. This implies that, during emplacement of the Packsaddle Basalts, the last fluids and melts from the Phoenix Plate were injected into the

mantle wedge at sub-arc depths. Because subduction was highly oblique, the northern edge of the Phoenix Plate moved nearly parallel to the margin beneath the arc, supplying the subduction component during that interval (see figures 2 and 9). This was likely accompanied by an anomalously high thermal gradient caused by the continuous presence of the slab window immediately to the north.

Comparison with magmatic suites produced during subduction of the Chile Ridge in the Patagonian domain north of this region reveals striking similarities. Five suites have been recognized before, during, and after opening of the Chile Ridge slab window (Ramírez-de-Arellano et al., 2021). Three of these suites are considered here for discussion. The first suite is "normal" medium-K calc-alkaline, recorded in the batholith and satellite plutons (Hervé et al., 2007; Ramírez-de-Arellano et al., 2012). The second suite is "transitional" magmatism that becomes progressively richer in alkalis as the slab window approaches, marking a shift from typical arc signatures toward intraplate-like compositions (e.g., Gorring et al., 1997; D'Orazio et al., 2004; Guivel et al., 2006; Corbella and Lara, 2008). Coevally, the third suite corresponds to volcanic and subvolcanic andesites with high Sr/Y ratios, previously reported along the arc domain (Kay et al., 1993; Ramos et al., 2004). These three suites correlate well with the PVC sub-units (see figures 5 and 6).

The plutonic rocks from Hardy Peninsula can be interpreted as a mafic member of the Palaeogene Seno de Año Nuevo Group defined by Suárez et al. (1985). The micro-gabbro sample FC2349 from Hardy Peninsula also exhibits a signature consistent with "normal" medium-K calc-alkaline Suite 1. However, in the absence of stratigraphic or geochronological constraints, its origin remains ambiguous: it could belong to a younger Neogene volcanic unit or represent a Palaeogene dike crosscutting the folded Jurassic to Cretaceous successions. If it is a Neogene volcanic unit, it would constitute the third (and oldest) member of the PVC.

437 The chemistry of the Pacha Dacites conforms to the calc-alkaline series, but with characteristic high
438 Sr/Y, low K/Na ratios (Fig. 5B, C), relatively high Mg# for a given SiO_2, and low concentrations of HREE
439 (Dy to Lu; see figure 6). These features closely resemble Suite 3 of the Patagonian domain (Figs. 5
440 and 6). On the other hand, the transitional signatures of the Packsaddle Basalts fit well with Suite 2
441 (Figs. 5 and 6). Their alkaline to subalkaline character, with FeO/MgO ratios near the tholeiitic–
442 calc-alkaline boundary and transitional trace-element ratios, intermediate between arc-related and
443 intraplate (OIB-like) signatures, are also characteristic of subduction-related primary melts termed
444 "low-SiO_2 basalts" (Schmidt and Jagoutz, 2017; see figure 5).

445 One crucial observation is that, whereas in the Patagonian domain, associated with subduction of
446 the Chile Ridge, the transitional magmatism occurred coevally with the high Sr/Y andesites, in the
447 Fuegian domain, associated with subduction of the NAZ-PHO ridge, field observations and available
448 geochronology indicate that the Sr/Y andesite-dacites occurred slightly before the transitional
449 basaltic magmatism. Nevertheless, in both cases a more detailed geochronological study is required
450 to precisely determine the lifespans and the relative timing of the magmatic episodes.

451

452 ***Bimodal arc-like magmatism related to oceanic ridge subduction***

453 Several features of the Pacha Dacites and Packsaddle Basalts can be attributed to the subduction of
454 the NAZ-PHO ridge and the approach of the related slab window to the sub-arc depths. Despite the
455 differences between them, their similar REE patterns (relatively high La/Yb and low Dy/Yb) suggest
456 that their primary melts formed at comparable depths, above the garnet-lherzolite stability field.
457 Very little interaction with the continental crust for the Packsaddle Basalts is shown by their primitive
458 geochemical and isotopic features. In the case of the Pacha Dacites, their chemistry implies deep-
459 seated fractionation. Therefore, their isotopic signature can be attributed to minor lower crustal

460 contamination or source contamination. Low interaction with the mid to upper continental crust and
461 therefore a rapid ascent is suggested in both cases, which can be attributed to an extensional regime
462 triggered by the NAZ-PHO spreading ridge at sub-arc depths (Fig. 9).

463 The contrasting alkalinity of these two PVC units, together with their different concentrations of REE,
464 implies substantially different degrees of mantle melting. The subalkaline magmatism of the Pacha
465 Dacites is typically associated with high degrees of mantle melting, due to metasomatism of the
466 mantle wedge, and is consistent with high concentrations of fluid mobile elements like U and Pb. An
467 alkaline magma series, such as the Packsaddle Basalts, implies lower degrees of partial melting,
468 concentrating alkalis and other incompatible elements like REE, but lower U and Pb anomalies. The
469 lower melting degrees inferred for the Packsaddle Basalts could be attributed to a rise of the mantle
470 solidus caused by a progressively decreasing flux of slab-derived fluids and melts. This interpretation
471 is consistent with the tectonic setting, given that the subducted Phoenix Plate supplied its final fluid-
472 melts prior to the opening of the NAZ-PHO slab window and the cessation of arc magmatism (see
473 figure 9).

474 Finally, the trace-element signature of the Packsaddle Basalts, notably the attenuated negative HFSE
475 anomaly relative to LILE, as shown, for instance, by the low Ba/Nb ratios (<30), suggests an
476 anomalously high thermal gradient. HFSE enrichment is commonly attributed to mantle re-
477 fertilization at intraplate mantle sources, where elevated temperatures destabilize rutile (e.g., Zheng
478 2019). The Packsaddle Basalts chemistry suggests that Nb and Ta were released into the mantle
479 wedge while fluids/melts were still acting as metasomatic agents at sub-arc depths. This may reflect
480 early destabilization of refractory phases, like rutile or clinohumite, in metasomatized domains at
481 the slab-mantle interface. Enhanced heat flow from a nearby slab window, as observed in the Chile
482 Ridge case (e.g., Sanhueza et al., 2023), could raise temperatures at the slab-mantle interface above
483 typical values (e.g., Syracuse et al., 2010), allowing metasomatism to proceed under conditions

484 where rutile is not stable (pressures ≲1.5 GPa or temperatures ≳1000 °C; Xiong et al., 2005; Skora
485 and Blundy, 2010; see figure 9). Further detailed study of these magmas would improve constraints
486 on thermodynamic conditions and metasomatic processes from sub-arc to greater depths.

487

488 **Conclusions**

489 This study documents a bimodal magmatic association in the Packsaddle Volcanic Complex (PVC)
490 through the integration of U-Pb zircon geochronology, whole-rock geochemistry, and Sr-Nd isotopic
491 data. U-Pb dating of a dacitic clast (20.5±0.2 Ma) confirms the Early Miocene (Aquitanian-
492 Burdigalian) age of high Sr/Y intermediate magmatism. Field observations demonstrate that this
493 magmatism preceded mildly alkaline basaltic activity, indicating a temporal evolution rather than
494 coeval bimodal volcanism.

495 The Pacha Dacites in the PVC show calc-alkaline signatures with high Sr/Y ratios and low HREE
496 contents, consistent with deep differentiation of hydrous intermediate magmas dominated by
497 amphibole fractionation. In contrast, the Packsaddle Basalts represent relatively Primitive Mantle-
498 derived melts, characterized by low SiO_2, high Mg#, and transitional arc to intraplate geochemical
499 affinities. Their Sr-Nd isotopic compositions indicate limited crustal assimilation. These contrasting
500 magmatic suites reflect a shift in the thermal and geodynamic regime of the subduction zone. Early
501 intermediate calc-alkaline magmatism formed under conditions with strong slab-derived input,
502 whereas later basaltic magmatism records reduced slab influence, lower degrees of melting, and
503 higher thermal gradients.

504 We interpret these magmatic suites as the result of ridge subduction and slab window development,
505 which modified the thermal structure of the mantle wedge and resulted in a shift from arc-like to
506 more intraplate-like compositions.

Acknowledgements

The Packsaddle Island is one of more than hundred *Geosites* identified by the Sociedad Geológica de Chile. This program was leaded by Pancho Hervé during its participation as Director, to identify and valorise the geological heritage of Chile. The new data reported here were funded by FONDECYT project N°1211906 (Chile). The authors thank the students and colleagues involved in the field seasons for their constructive discussion. The authors also thank Capitán Hugo Cárdenas and the crew of Huracán. Constructive comments from Malcolm Hole and an anonymous reviewer improved this manuscript. Bob Pankhurst, as Guest Editor, and Daniel Bertin, as Editor-in-Chief, further enhanced it with their recommendations.

References

Alonso-Perez, R., Müntener, O., & Ulmer, P. (2009). Igneous garnet and amphibole fractionation in the roots of island arcs: experimental constraints on andesitic liquids. *Contributions to Mineralogy and Petrology*, *157*(4), 541–558. https://doi.org/10.1007/s00410-008-0351-8

Black, L., Kamo, S., Allen, C. M., Aleinikoff, J., Davis, D., Korsch, R. & Foudoulis, C. (2003). TEMORA 1: A new zircon standard for Phanerozoic U-Pb geochronology. Chemical Geology, 200, 155–170. https://doi.org/10.1016/s0009-2541(03)00165-7

Breitsprecher, K. & Thorkelson, D. J. (2009). Neogene kinematic history of Nazca–Antarctic–Phoenix slab windows beneath Patagonia and the Antarctic Peninsula. *Tectonophysics*, *464*(1–4), 10–20. https://doi.org/10.1016/j.tecto.2008.02.013

Calderón, M., Fildani, A., Herve, F., Fanning, C. M., Weislogel, A., & Cordani, U. (2007). Late Jurassic bimodal magmatism in the northern sea-floor remnant of the Rocas Verdes basin, southern Patagonian Andes. Journal of the Geological Society, 164(5), 1011-1022. https://doi.org/10.1144/0016-76492006-102

Cande, S. C. & Leslie, R. B. (1986). Late Cenozoic tectonics of the Southern Chile Trench. *Journal of Geophysical Research: Solid Earth*, *91*(B1), 471–496. https://doi.org/10.1029/jb091ib01p00471

Corbella, H. & Lara, L. E. (2008). Late Cenozoic Quaternary Volcanism in Patagonia and Tierra del Fuego. In ["J. Rabassa"] (Ed.), *The Late Cenozoic of Patagonia and Tierra del Fuego* (Vol. 11, pp. 95–119). Elsevier. https://doi.org/10.1016/s1571-0866(07)10006-3

Dalziel, I., de Wit, M. & Palmer, K. Fossil marginal basin in the southern Andes. Nature 250, 291–294 (1974). https://doi.org/10.1038/250291a0

Davidson, J., Turner, S., Handley, H., Macpherson, C. & Dosseto, A. (2007). Amphibole "sponge" in arc crust? *Geology*, *35*(9), 787–790. https://doi.org/10.1130/g23637a.1

Defant, M., Drummond, M. (1990) Derivation of some modern arc magmas by melting of young subducted lithosphere. Nature 347, 662–665. https://doi.org/10.1038/347662a0

D'Orazio;, M., Innocent, F., Manetti, P. & Haller, M. J. (2004). Cenozoic back-arc magmatism of the southernextra-Andean Patagonia (44° 30' - 52° S): A review ofgeochemical data and geodynamic interpretations. *Revista de La Asociación Geológica Argentina*, *59*(4), 525–538.

Eagles, G. & Jokat, W. (2014). Tectonic reconstructions for paleobathymetry in Drake Passage. *Tectonophysics*, *611*, 28–50. https://doi.org/10.1016/j.tecto.2013.11.021

Eagles, G. & Scott, B. G. C. (2014). Plate convergence west of Patagonia and the Antarctic Peninsula since 61Ma. *Global and Planetary Change*, *123*, 189–198. https://doi.org/10.1016/j.gloplacha.2014.08.002

Espinoza, F., Morata, D., Polve, M., Lagabrielle, Y., Maury, R., Rupelle, A. de la, Guivel, C., Cotten, J., Bellon, H., & Suarez, M. (2010). Middle Miocene calc-alkaline volcanism in Central Patagonia (47·S): petrogenesis and implications for slab dynamics. Andean Geology, 37(2), 300–328. https://doi.org/10.5027/andgeov37n2-a03

Gaetani, G., Grove, T. & Bryan, W. The influence of water on the petrogenesis of subductionrelated igneous rocks. Nature 365, 332–334 (1993). https://doi.org/10.1038/365332a0

Gao, Y., O'Neill, H. S. C. & Mavrogenes, J. A. (2023). Garnet versus amphibole: Implications for magmatic differentiation and slab melting. *Geology*, *52*(2), 125–129. https://doi.org/10.1130/g51637.1

Goldsmith, J. (1982). Plagioclase stability at elevated temperatures and water pressures. American Mineralogist, 67 (7-8): 653–675.

Gómez-Tuena, A., Cavazos-Tovar, J. G., Parolari, M., Straub, S. M. & Espinasa-Pereña, R. (2018). Geochronological and geochemical evidence of continental crust 'relamination' in the origin of intermediate arc magmas. *Lithos*, *322*, 52–66. https://doi.org/10.1016/j.lithos.2018.10.005

Gorring, M.L., Kay, S.M., 2001. Mantle processes and sources of Neogene slab window magmas from Southern Patagonia, Argentina. J. Petrol. 42, 1067e1094.

Gorring, M. L., Kay, S. M., Zeitler, P. K., Ramos, V. A., Rubiolo, D., Fernandez, M. I. & Panza, J. L. (1997). Neogene Patagonian plateau lavas: Continental magmas associated with ridge collision at the Chile Triple Junction. *Tectonics*, *16*(1), 1–17. https://doi.org/10.1029/96tc03368

Guivel, Christèle, Morata, D., Pelleter, E., Espinoza, F., Maury, R. C., Lagabrielle, Y., Polvé, M., Bellon, H., Cotten, J., Benoit, M., Suárez, M. & Cruz, R. de la. (2006). Miocene to Late Quaternary Patagonian basalts (46–47°S): Geochronometric and geochemical evidence for slab tearing due to active spreading ridge subduction. *Journal of Volcanology and Geothermal Research*, *149*(3–4), 346–370. https://doi.org/10.1016/j.jvolgeores.2005.09.002

Hervé, F., Pankhurst, R. J., Fanning, C. M., Calderón, M. & Yaxley, G. M. (2007). The South Patagonian batholith: 150 my of granite magmatism on a plate margin. *Lithos*, *97*(3–4), 373–394. https://doi.org/10.1016/j.lithos.2007.01.007

Hervé, M., Suárez, M. & Puig, A. (1984). The Patagonian Batholith S of Tierra del Fuego, Chile: timing and tectonic implications. *Journal of the Geological Society*, *141*(5), 909–917. https://doi.org/10.1144/gsjgs.141.5.0909

Hole, M.J., 2021, Antarctic Peninsula: Petrology, in Smellie, J.L., et al., eds., Volcanism in Antarctica: 200 Million Years of Subduction, Rifting and Continental Break-Up: Geological Society, London, Memoir 55, 327–343. https://doi.org/10.1144/M55-2018-40

Hole, M., Gibson, S., Morris,. M. (2023) Slab window–related magmatism as a probe for pyroxenite heterogeneities in the upper mantle. *Geology* *51* (3), 268–272. https://doi.org/10.1130/G50687.1

Hickey-Vargas, R., Holbik, S., Tormey, D., Frey, F. & Moreno, H. (2016). Basaltic rocks from the Andean Southern Volcanic Zone: Insights from the comparison of along-strike and small-scale geochemical variations and their sources. *Lithos*, 258–259, 115–132. https://doi.org/10.1016/j.lithos.2016.04.014

Irvine, T. N. & Baragar, W. R. A. (1971). A Guide to the Chemical Classification of the Common Volcanic Rocks. *Canadian Journal of Earth Sciences*, *8*(5), 523–548. https://doi.org/10.1139/e71-055

Kay, S., Ramos, V. & Marquez, M. J. (1993). Evidence in Cerro Pampa Volcanic Rocks for Slab-Melting Prior to Ridge-Trench Collision in Southern South America. *The Journal of Geology*, *101*, 703–714. https://doi.org/10.1086/648269

Kilian, R., & Behrmann, J. H. (2003). Geochemical constraints on the sources of southern Chile Trench sediments and their recycling in arc magmas of the southern Andes. *Journal of the Geological Society, 160*(1), 57–70. https://doi.org/10.1144/0016-764901-143

Ludwig, K.R. (2000) SQUID 1.00, a user's manual. Berkeley Geochronology Center Special Publication, Berkeley.

Moyen, J.-F. (2009). High Sr/Y and La/Yb ratios: The meaning of the "adakitic signature." Lithos, 112(3–4), 556–574. https://doi.org/10.1016/j.lithos.2009.04.001

Muller, V. A. P., Sue, C., Valla, P. G., Sternai, P., Simon-Labric, T., Gautheron, C., Cuffey, K. M., Grujic, D., Bernet, M., Martinod, J., Ghiglione, M. C., Reiners, P., Willett, C., Shuster, D., Herman, F., Baumgartner, L. & Braun, J. (2024). Geodynamic and Climatic Forcing on Late-Cenozoic Exhumation of the Southern Patagonian Andes (Fitz Roy and Torres del Paine massifs). *Tectonics*, *43*(7). https://doi.org/10.1029/2023tc007914

Müntener, O., Kelemen, P. B. & Grove, T. L. (2001). The role of H_2O during crystallization of primitive arc magmas under uppermost mantle conditions and genesis of igneous pyroxenites: an experimental study. Contributions to Mineralogy and Petrology 141, 643–658.

Nandedkar, R. H., Ulmer, P. & Müntener, O. (2014). Fractional crystallization of primitive hydrous arc magmas: an experimental study at 07 GPa. Contributions to Mineralogy and Petrology 167, 1015, https://doi.org/10.1007/s00410-014-1015-5.

Nandedkar, R. H., Hürlimann, N., Ulmer, P. & Müntener, O. (2016). Amphibole–melt trace element partitioning of fractionating calc-alkaline magmas in the lower crust: an experimental study. *Contributions to Mineralogy and Petrology*, *171*(8–9), 71. https://doi.org/10.1007/s00410-016-1278-0

Nullo, F., Proserpio, C., Ramos, V. & Rabassa, J. (1978). *Estratigrafía y tectónica de la vertiente este del hielo continental patagónico, Argentina-Chile*. *1*, 455–470.

Orihashi, Y., Anma, R., Motoki, A., Haller, M., Hirata, D., Iwnao, H., Sumino, H. & Ramos, V. (2013). *Evolution history of the crust underlying Cerro Pampa, Argentine Patagonia: Constraint from LA-ICPMS U-Pb ages for exotic zircons in the Mid-Miocene adakite*. 037. https://doi.org/10.14863/geosocabst.2013.0_037

Palme, H. & O'Neill, H. St. C. (2014). *Treatise on Geochemistry (Second Edition)*. 1–39. https://doi.org/10.1016/b978-0-08-095975-7.00201-1

Pardo-Casas, F. & Molnar, P. (1987). Relative motion of the Nazca (Farallon) and South American Plates since Late Cretaceous time. *Tectonics*, *6*(3), 233–248. https://doi.org/10.1029/tc006i003p00233

Puig, A., Herve, M., Suarez, M. & Saunders, A. D. (1984). Calc-alkaline and alkaline miocene and calc-alkaline recent volcanism in the Southernmost Patagonian Cordillera, Chile. *Journal of Volcanology and Geothermal Research*, *21*(1–2), 149–163. https://doi.org/10.1016/0377-0273(84)90020-9

Ramírez-de-Arellano, C., Calderón, M., Rivera, H., Valenzuela, M., Fanning, C. M. & Paredes, E. (2021). Neogene Patagonian magmatism between the rupture of the Farallon plate and the Chile Ridge subduction. *Journal of South American Earth Sciences*, *110*, 103238. https://doi.org/10.1016/j.jsames.2021.103238

Ramírez-de-Arellano, C., Putlitz, B., Müntener, O. & Ovtcharova, M. (2012). High precision U/Pb zircon dating of the Chaltén Plutonic Complex (Cerro Fitz Roy, Patagonia) and its relationship to arc migration in the southernmost Andes. *Tectonics*, *31*(4). https://doi.org/10.1029/2011tc003048

Ramos, V., Kay, S. & Singer, B. (2004). The adakites of the Patagonian Cordillera: New geochemical and geochronological evidences. *Revista de La Asociación Geológica Argentina*, *59*(4), 693–706.

Ramos, V. A. (2005). Seismic ridge subduction and topography: Foreland deformation in the Patagonian Andes. *Tectonophysics*, *399*(1–4), 73–86. https://doi.org/10.1016/j.tecto.2004.12.016

Ramos, V. A. & Kay, S. M. (1992). Southern Patagonian plateau basalts and deformation: Backarc testimony of ridge collisions. *Tectonophysics*, *205*(1–3), 261–282. https://doi.org/10.1016/0040-1951(92)90430-e

Ricci, C., Hervé, F., Krinauw, J., & Lemasurier, W. (1993). Naming of igneous and metamorphic rock units in Antarctica: recommendation by the SCAR Working Group on Geology. Antarctic Science 5 (1): 103-104.

Salters, V.J.M. & Stracke, A. (2004). Composition of the depleted mantle. *Geochemistry, Geophysics, Geosystems*, *5*(5). https://doi.org/10.1029/2003GC000597

Sanhueza, J., Yáñez, G., Buck, W. R., Vargas, J. A., & Veloso, E. (2023). Ridge Subduction: Unraveling the Consequences Linked to a Slab Window Development Beneath South America at the Chile Triple Junction. Geochemistry, Geophysics, Geosystems, 24(9). https://doi.org/10.1029/2023gc010977

Schmidt, M. W. & Jagoutz, O. (2017). The global systematics of primitive arc melts. *Geochemistry, Geophysics, Geosystems*, *18*(8), 2817–2854. https://doi.org/10.1002/2016gc006699

Skora, S., Blundy, J. (2010). High-pressure Hydrous Phase Relations of Radiolarian Clay and Implications for the Involvement of Subducted Sediment in Arc Magmatism. J. Petrol., 51(11), 2211–2243. https://doi.org/10.1093/petrology/egq054

Stern, C., & Wit, M. J. (2003). Rocas Verdes ophiolites, southernmost South America: Remnants of progressive stages of development of oceanic-type crust in a continental margin back-arc basin. Geological Society, London, Special Publications, 218, 665–683. https://doi.org/10.1144/gsl.sp.2003.218.01.32

Stevens-Goddard, A. L. & Fosdick, J. C. (2019). Multichronometer thermochronologic modeling of migrating spreading ridge subduction in southern Patagonia. *Geology*, *47*(6), 555–558. https://doi.org/10.1130/g46091.1

Suárez, M., Hervé, M. & Puig, Á. (1985). *Carta Geológica de Chile 1: 250.000, Hoja Isla Hoste e Islas Adyacentes*. SERNAGEOMIN, Chile, 1985.

671 Syracuse, E. M., Keken, P. E. van, & Abers, G. A. (2010). The global range of subduction zone thermal
672 models. Physics of the Earth and Planetary Interiors, 183(1–2), 73–90.
673 https://doi.org/10.1016/j.pepi.2010.02.004

674 Tera, F. & Wasserburg, G. J. (1972). U-Th-Pb systematics in three Apollo 14 basalts and the problem
675 of initial Pb in lunar rocks. Earth and Planetary Science Letters, 14(3), 281–304.
676 https://doi.org/10.1016/0012-821x(72)90128-8

677 Wang, X., Sun, M., Weinberg, R. F., Cai, K., Zhao, G., Xia, X., Li, P. & Liu, X. (2022). Adakite generation
678 as a result of fluid-fluxed melting at normal lower crustal pressures. *Earth and Planetary Science*
679 *Letters*, *594*, 117744. https://doi.org/10.1016/j.epsl.2022.117744

680 Williams, I. (1998). U-Th-Pb geochronology by ion microprobe: Reviews in Economic Geology, v. 7.

681 Wilson, M. (1989). *Igneous Petrogenesis*. Springer Dordrecht. https://doi.org/10.1007/978-1-4020-
682 6788-4

683 Xiong, X. L., Adam, J. & Green, T. H. (2005). Rutile stability and rutile/melt HFSE partitioning during
684 partial melting of hydrous basalt: Implications for TTG genesis. *Chemical Geology*, *218*(3–4), 339–
685 359. https://doi.org/10.1016/j.chemgeo.2005.01.014

686 Xu, J.-F. & Chen, S.-S. (2023). Petrogenesis of adakitic rocks unrelated to slab melting and adakitic
687 porphyries associated with Cu mineralization. *Lithos*, *458*, 107351.
688 https://doi.org/10.1016/j.lithos.2023.107351

689 Yang, S., Su, L., Song, S., Allen, M. B., Feng, D., Wang, M., Wang, C. & Zhang, H. (2020). Melting of
690 subducted continental crust during collision and exhumation: Insights from granitic rocks from
691 the North Qaidam UHP metamorphic belt, NW China. *Lithos*, *378*, 105794.
692 https://doi.org/10.1016/j.lithos.2020.105794

693 Yogodzinski, G. M., Lees, J. M., Churikova, T. G., Dorendorf, F., Wöerner, G. & Volynets, O. N. (2001).
694 Geochemical evidence for the melting of subducting oceanic lithosphere at plate edges. *Nature*,
695 *409*(6819), 500–504. https://doi.org/10.1038/35054039

696 Zhang, L., Li, S. & Zhao, (2021). A review of research on adakites. *International Geology Review*, *63*(1),
697 47–64. https://doi.org/10.1080/00206814.2019.1702592

698 Zheng, Y.-F. (2019). Subduction zone geochemistry. Geoscience Frontiers, 10, 1223–1254.

699 Zhen, Z., dong, X. & Lintao, Z. (2025). A slab window in the south rim of the Parece-Vela Basin.
700 *Scientific Reports*, *15*(1), 2387. https://doi.org/10.1038/s41598-025-86913-z

701

702

703

704 **Figure captions**

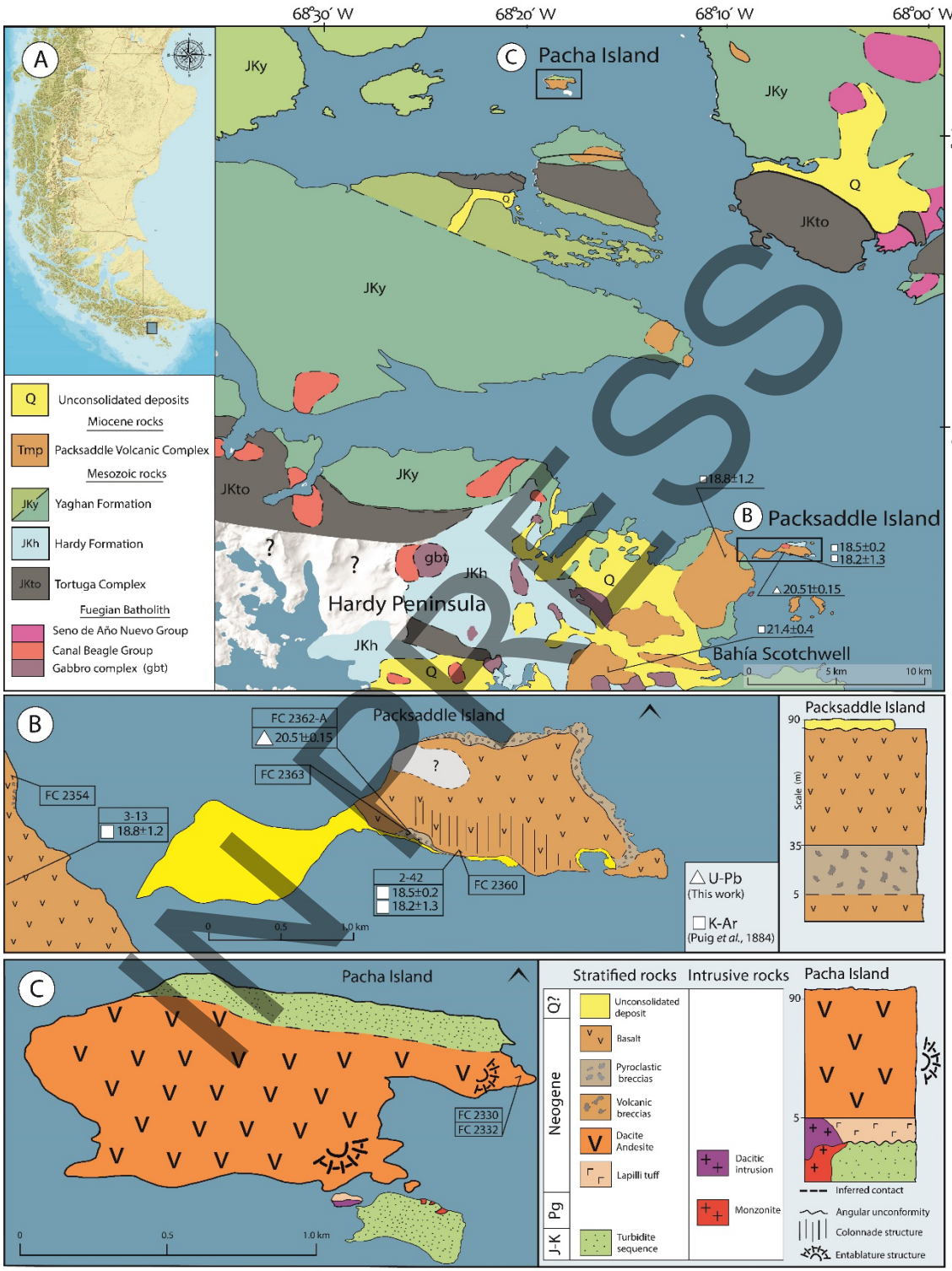

705

706 **Fig. 1.** Geological map of Packsaddle and Pacha islands and surrounding areas. **A** is after Suárez et
707 al. (1985) with regional units and locations of samples dated by Puig et al. (1984). **B** and **C** are
708 lithological maps produced in this work, with location of samples used for geochemistry and U-Pb
709 SHRIMP zircon dating; schematic stratigraphic columns are shown to the right. All ages in Ma.

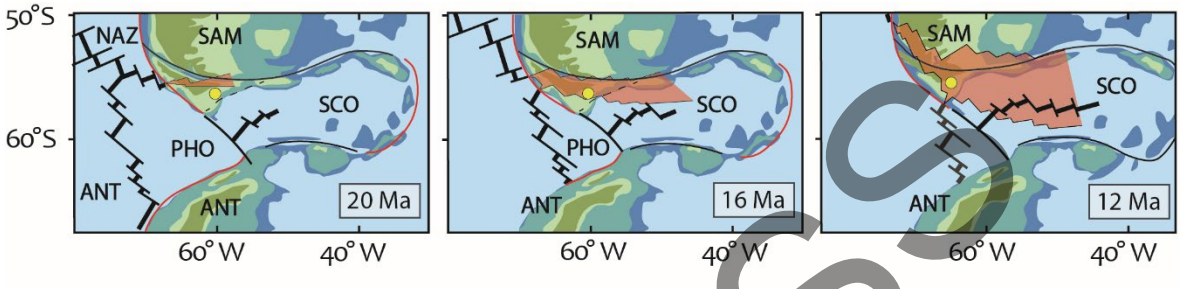

710

711 **Fig. 2.** Plate-tectonic evolution of the Fuegian region in southernmost South America after Eagle and
712 Jokat (2014), showing subduction of the Nazca (NAZ), Phoenix (PHO), and Antarctic (ANT) plates
713 beneath the South America (SAM) and Scotia (SCO) plates at 20, 16, and 12 Ma. The slab window
714 (brownish red domain) follows Breitsprecher and Thorkelson (2009). The yellow circle marks the
715 study area: at 20 Ma it laid above the Phoenix Plate slab, whereas by 16 and 12 Ma it laid above the
716 slab window.

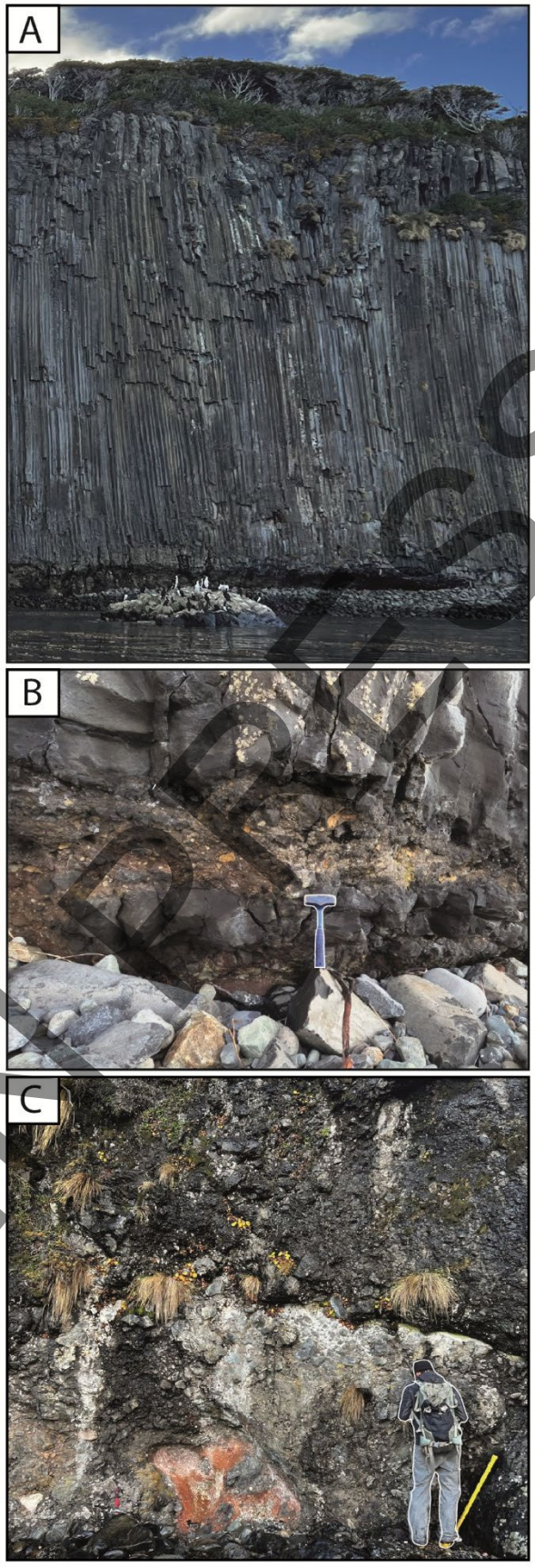

718 **Fig. 3.** Field observations on Packsaddle Island. **A.** Columnar jointing in the main basalt sill. **B.** Detail
719 of the contact between the lower breccia and the overlying basalt, showing the basalt crosscutting
720 the breccia. **C.** Lower pyroclastic breccia, which locally reaches up to 30 m thickness; note the block
721 sizes and distribution.

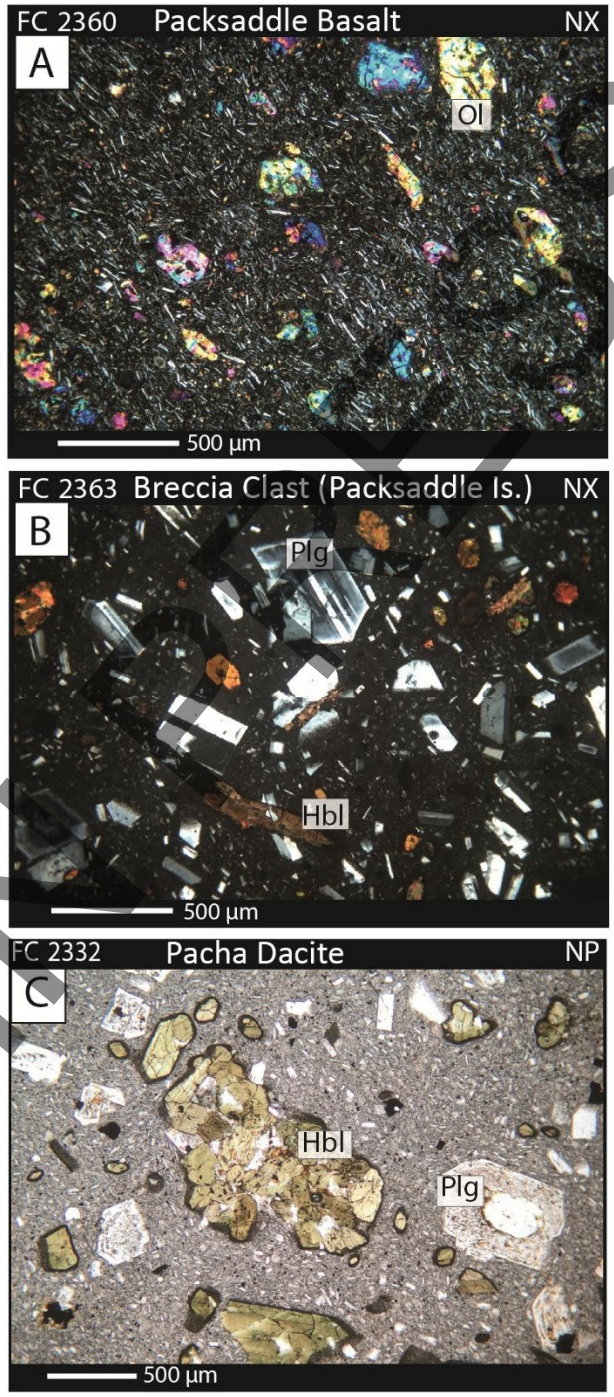

722

Fig. 4. Typical petrography of the Packsaddle Volcanic Complex. **A.** Olivine-basalt, Packsaddle Island. **B.** Dacite clast from the basal breccia, Packsaddle Island. **C.** Hornblende-dacite, Pacha Island. Hbl: Hornblende; Plg: Plagioclase. NX: Crossed nicols; NP: Parallel nicols. See figure 1 for sample locations.

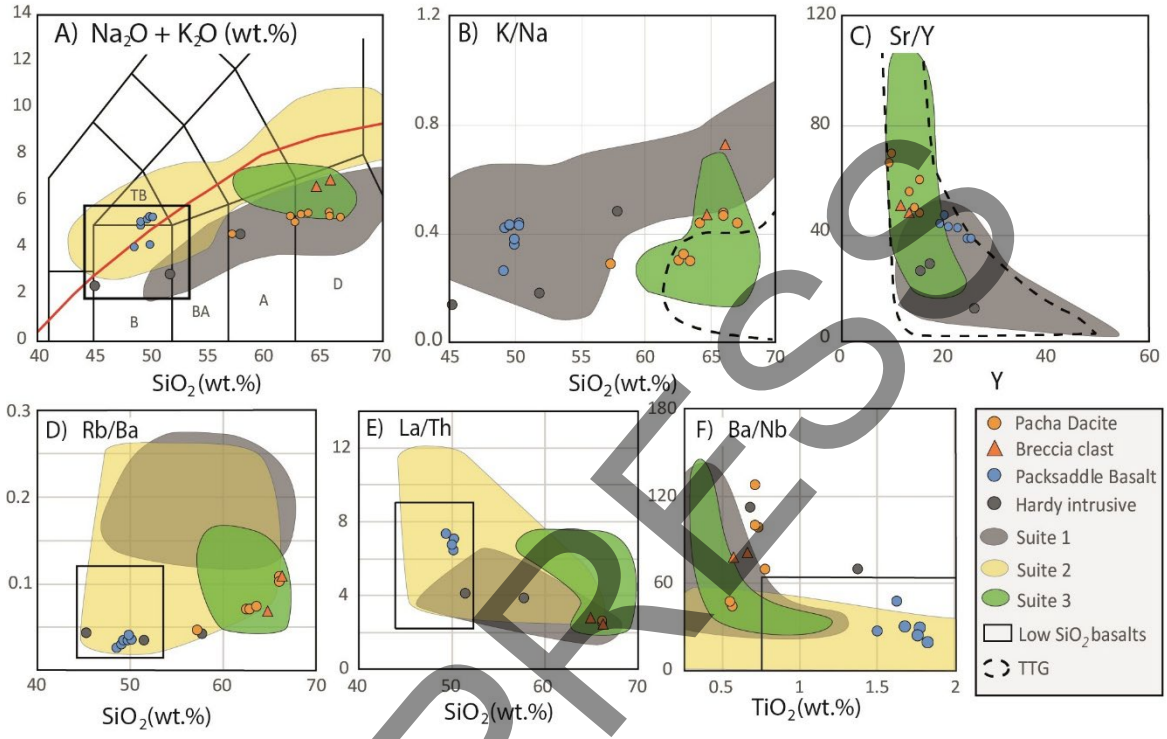

Fig. 5. Main geochemical features of Packsaddle Basalts (blue circles), Pacha Dacites (orange circles), plus two breccia clasts from Packsaddle Island (orange tringles), and Hardy Peninsula intrusives. **A.** TAS diagram with alkaline-subalkaline limit (red line) after Irvine and Baragar (1971). (TB: trachybasalt, B: basalt, BA: basaltic andesite, A: andesite, and D: dacite.) **B.** K/Na ratios vs. silica. **C.** Sr/Y vs. Y. **D** and **E** show Rb/Ba and La/Th ratios vs. silica. **F.** Ba/Nb ratios vs. TiO_2 (high values correlate with a HFSE negative anomaly; low TiO_2 denotes negative Ti anomaly relative to HREE; see also figure 6). Suites 1, 2, and 3 represent the Neogene Patagonian magmatism north of 53° S (Ramírez-de-Arellano et al., 2021). Suite 1 (grey area) corresponds to the Neogene calc-alkaline South Patagonian Batholith, exemplifying typical Andean magmatism; Suite 2 (yellow area) includes slightly alkaline rocks formed immediately before the opening of the slab window; Suite 3 (green area) corresponds

volcanic to subvolcanic high Sr/Y andesites coeval with Suite 2. Note the similarities of Packsaddle Basalts with Suite 2 and Pacha Dacites with Suite 3, as well as between the Packsaddle Basalts and the low-silica primary basalts (black frame rectangles) from the global compilation of subduction-related primary magmas by Schmidt and Yagoutz (2017). Conversely, the Pacha Dacites correlate well with the Archean TTG Suite (dashed black lines in panels B and C), as an ancient analogue of hot subduction magmatism.

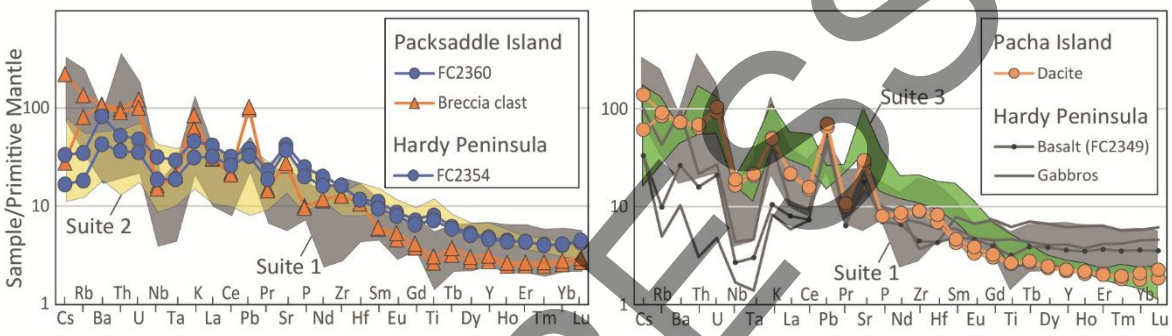

Fig. 6. Multi-element (spider) diagrams normalized to Primitive Mantle (Palme and O'Neill, 2014) for representative samples from Packsaddle and Pacha islands and Hardy Peninsula. Fields are shown for Neogene Patagonian Suites 1 (grey), 2 (yellow), and 3 (green), as in figure 5.

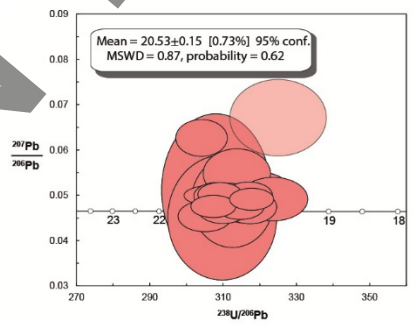

Fig. 7. Concordia plot of zircon U-Pb SHRIMP data for sample FC2362-A, a dacitic tuff clast from the basal breccia on Packsaddle Island. The pale shaded ellipse is for analysis 22.1 (not used in the age calculation). MSWD: mean square weighted deviation.

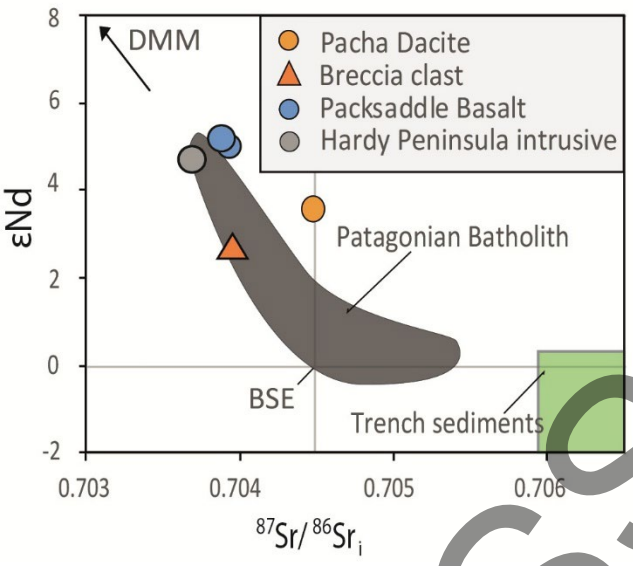

751

752 **Fig. 8.** εNd vs. $^{87}Sr/^{86}Sr$ diagram for the Pacha Dacites and Packsaddle Basalts. The grey field
753 represents the Patagonian Batholith (Hervé et al., 2007), which corresponds to Suite 1 (see figures 5
754 and 6). Isotopic composition from Depleted MORB Mantle (DMM) according to Salters and Stracke
755 (2004). Trench sediments after Kilian and Behrmann (2003). BSE: Bulk Silicate Earth isotopic
756 composition at present.

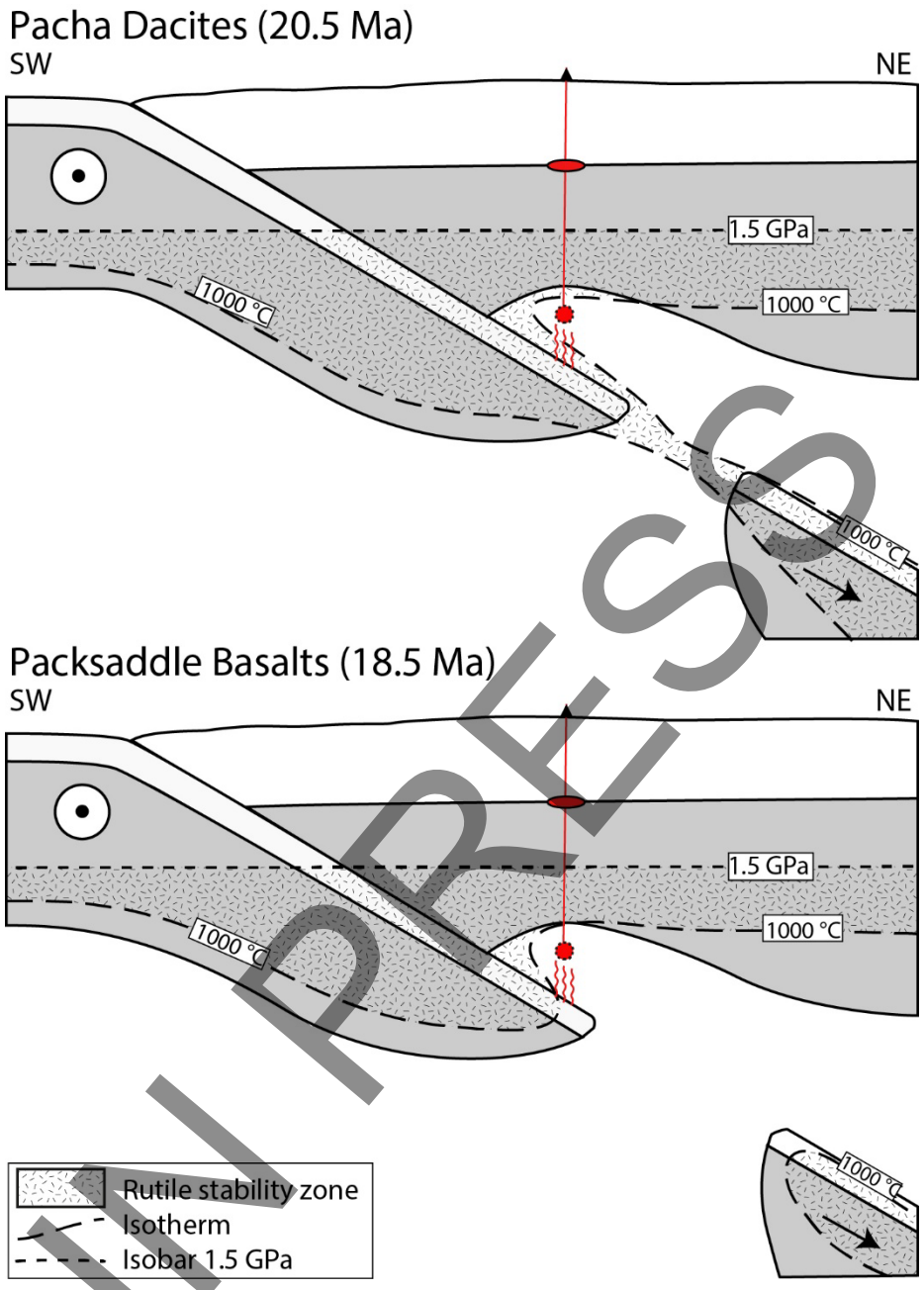

Fig. 9. Schematic subduction profile along a SW-NE section perpendicular to the margin in the Fuegian domain, where Packsaddle Island is located, at the time of formation of the PVC. Because the Phoenix-Scotia convergence vector is almost parallel to the margin (see figure 2), the Phoenix slab appears effectively stationary beneath the arc, whereas the Nazca slab is migrating slowly

762 northward. Before the opening of the slab window beneath the arc, the 1000 °C isotherm splits

763 toward both slabs, promoting rutile destabilization and the transfer of Na-Ta into the mantle wedge.

764

765 **TABLES**

Table 1. Whole-rock geochemistry of the Packsaddle Volcanic Complex.

Locality	Packsaddle Island							Pacha Island		Hardy Peninsula									
Sample N°	FC2362-A	FC2363	FC2360	11TU-580	11TU-5808	2-42	686	FC2330	FC2332	FC2349	FC2351	FC2352	FC2354	3-13	3-12-c	3-14	3-15	182	523-1	1-51
Rock type	Dacite clast	Dacite clast	Ol-basalt	Basalt	Basalt	Basalt	Basalt	Dacite	Dacite	Micro-gabbro	Diorite	Gabbro	Ol-basalt	Basalt	Andesite	Andesite	Dacite	Dacite	Dacite	Dacite
Latitude	55,402	55,402	55,403	55,4	55,4			55,13	55,128	55,427	55,421	55,421	55,396							
Longitude	68,080	68,080	68,138	68,1	68,1			68,289	68,287	68,114	68,111	68,111	68,138							
Reference*	This work	This work	This work	R.2021	R.2021	P.1984	P.1984	This work	This work	This work	This work	This work	This work	P.1984	P.1984	P.1984	P.1984	P.1984	P.1984	P.1984
SiO_2 [wt.%]	66,18	64,81	50,21	49,89	49,22	49,67	50,21	66,02	66,07	51,55	57,80	45,11	50,02	49,10	62,94	62,58	63,53	67,02	64,18	57,27
TiO_2 [wt.%]	0,57	0,66	1,72	1,80	1,81	1,89	1,83	0,57	0,58	0,70	0,61	1,40	1,54	1,68	0,74	0,72	0,73	0,60	0,83	0,79
Al_2O_3 [wt.%]	17,47	17,74	15,56	16,04	16,30	15,97	16,03	16,69	16,46	17,05	18,32	16,77	16,41	17,06	18,77	18,87	18,92	16,93	17,75	18,15
FeO* [wt.%]	3,45	4,13	8,27	8,27	8,63	8,22	7,93	3,97	3,81	8,22	7,13	12,27	8,34	9,04	4,51	4,49	4,27	3,48	4,72	6,29
MnO [wt.%]	0,08	0,08	0,20	0,17	0,19	0,23	0,16	0,05	0,08	0,33	0,22	0,27	0,15	0,18	0,12	0,10	0,10	0,08	0,15	0,13
MgO [wt.%]	1,17	1,39	9,02	8,78	8,93	9,21	8,83	2,07	2,00	8,62	3,31	8,70	9,62	7,94	1,97	1,97	1,38	1,19	1,24	4,71
CaO [wt.%]	3,99	4,39	9,11	9,28	9,25	9,22	9,13	5,00	5,45	10,36	7,78	12,82	9,29	10,58	5,67	5,72	5,54	5,28	5,57	7,84
Na_2O [wt.%]	4,17	4,68	3,85	3,73	3,60	3,63	3,85	3,82	3,79	2,60	3,25	2,13	3,13	3,31	3,94	4,20	4,28	3,78	3,92	3,65
K_2O [wt.%]	2,72	1,94	1,47	1,53	1,51	1,41	1,52	1,63	1,59	0,35	1,40	0,26	1,01	0,77	1,14	1,13	1,14	1,49	1,55	0,94
P_2O_5 [wt.%]	0,21	0,19	0,51	0,52	0,57	0,49	0,51	0,17	0,16	0,15	0,17	0,20	0,41	0,30	0,20	0,20	0,10	0,15	0,10	0,20
LOI [wt.%]	2,44	1,07	1,1	1,5	1,62	1,86	0	3,29	2,74	2,91	3,71	1,28	2,67	1,84	1,78	1,91	2,36	0	0	0,93
Original Total	97,51	98,79	97,64	100,30	100,40	96,50	98,58	96,10	97,67	98,98	94,56	98,37	97,43	96,15	97,00	96,96	96,24	100,42	96,92	97,76
Sc [ppm]	5	7	24	25	24			8	8	31	15	50	26							
V [ppm]	92	52	227	216	221	196		75	76	230	160	491	210	197	83	86	84			126
Cr [ppm]	< 20	20	340	310	300	300		30	60	420	80	260	380	258	5	5	5			181
Co [ppm]	9	9	37	38	37			9	9	30	15	46	36							
Ni [ppm]	< 20	< 20	220	170	160	115		30	50	140	40	130	210	78	3	3	3			91
Cu [ppm]	20	30	80					30	30	120	40	10	70							
Zn [ppm]	50	40	60	70	70			50	60	200	80	120	70							
Ga [ppm]	17	17	16					16	17	16	16	17	16							
Ge [ppm]	1,2	1,3	1,2					0,9	1,1	1,4	0,9	1,6	1							
Rb [ppm]	82	49	21	18	18	16		51	55	6	26	3	11	11	35	35	37			23
Sr [ppm]	570	607	923	873	946	914		598	656	393	493	314	823	961	714	695	721			901
Y [ppm]	11	13	20	21	22	24		9	9	15	17	26	19	25	15	14	13			15
Zr [ppm]	133	131	166	161	175	174		92	94	46	71	38	167	141	103	102	101			87
Nb [ppm]	10	9	19	21	19	24		10	11	2	3	1	11	9	5	5	4			7
Cs [ppm]	4,0	0,5	0,6	0,8	0,7			1,1	2,5	0,6	1,8	0,6	0,3							
Ba [ppm]	745	730	566	513	574	469		496	500	181	648	71	293	425	490	497	509			485
La [ppm]	20,8	21,1	28,4	29,2	29,8	30,0		14,5	14,9	5,5	7,1	4,0	21,8	23,0	5,0	7,0	6,0			25,0
Ce [ppm]	38,7	36,8	55,9	58,7	59,5			26,3	27,9	12,9	16,3	12,7	45,6							
Pr [ppm]	4,02	3,84	6,15	6,68	6,83			2,72	2,87	1,70	2,05	1,92	4,99							
Nd [ppm]	15,3	15,8	26,7	26,1	25,9			10,7	11,6	8,9	10,1	11,6	21,6							
Sm [ppm]	2,55	2,62	4,81	4,78	4,97			1,86	2,02	2,13	2,58	3,43	4,10							
Eu [ppm]	0,76	0,88	1,43	1,67	1,80			0,56	0,65	0,77	0,80	1,12	1,32							
Gd [ppm]	2,14	2,42	4,17	3,88	4,15			1,78	1,90	2,24	2,69	4,20	3,76							
Tb [ppm]	0,34	0,40	0,66	0,67	0,67			0,29	0,30	0,42	0,47	0,76	0,63							
Dy [ppm]	1,97	2,19	3,82	4,02	4,07			1,72	1,79	2,78	2,94	4,82	3,64							
Ho [ppm]	0,39	0,42	0,71	0,75	0,76			0,33	0,35	0,56	0,60	1,01	0,69							
Er [ppm]	1,16	1,24	2,01	2,09	2,17			0,98	0,95	1,72	1,95	2,99	2,03							
Tm [ppm]	0,180	0,196	0,297	0,290	0,300			0,135	0,145	0,261	0,310	0,423	0,293							
Yb [ppm]	1,22	1,32	1,91	1,87	2,05			0,86	1,00	1,72	2,16	2,76	1,94							
Lu [ppm]	0,189	0,208	0,301	0,28	0,3			0,132	0,161	0,251	0,327	0,436	0,315							
Hf [ppm]	3,2	3,2	3,5	3,6	3,6			2,1	2,5	1,3	1,8	1,3	3,5							
Ta [ppm]	0,89	0,88	1,26	1,32	1,38			0,89	0,93	0,13	0,20	0,06	0,81							
Tl [ppm]	0,52	0,14	0,11					0,25	0,28	0,05	0,21	0,11	0,06							
Pb [ppm]	18	19	7	18	7			12	13	10	8	< 5	6							
Th [ppm]	8,34	7,66	4,44	4,31	4,06			5,44	5,83	1,35	1,83	0,26	3,09							
U [ppm]	2,81	2,3	1,1	1,11	1,09			2,1	2,38	0,48	0,62	0,11	0,81							
Mg#	0,38	0,37	0,66	0,65	0,65	0,67	0,66	0,48	0,48	0,65	0,45	0,56	0,67	0,61	0,44	0,44	0,37	0,38	0,32	0,57
K/Na	0,73	0,47	0,43	0,27	0,28	0,43	0,44	0,48	0,47	0,15	0,48	0,14	0,36	0,26	0,33	0,30	0,30	0,44	0,44	0,29
Sr/Y	50,4	47,1	46,6	42,4	42,2	38,1		65,7	69,8	26,4	29,0	12,3	43,5	38,4	47,6	49,6	55,5			60,1
Rb/Ba	0,11	0,07	0,04	0,04	0,03	0,03		0,10	0,11	0,03	0,04	0,04	0,04	0,03	0,07	0,07	0,07			0,05
Ba/Nb	76,8	81,1	29,9	24,0	29,6	19,5		50,6	44,2	113,1	249,2	71,0	26,4	47,2	98,0	99,4	127,3			69,3
Ce/Pb	2,2	1,9	8,0	3,3	8,5			2,2	2,1	1,3	2,0		7,6							
La/Th	2,49	2,75	6,40	6,77	7,34			2,67	2,56	4,05	3,87	15,46	7,06							

Notes:

*It includes previously published data from P.1984 (Puig et al., 1984) and R.2021 (Ramírez-de-Arellano et al., 2021).

The table also includes the element's ratios mentioned in the text.

Table 2. Summary of U-Pb SHRIMP zircon dating from sample FC2362-A.

Grain spot	U [ppm]	Th [ppm]	Th/U	$^{206}Pb^*$ [ppm]	$^{204}Pb/^{206}Pb$	f_{208} [%]	Total				Radiogenic		Age [Ma]	
							$^{238}U/^{206}Pb$	±	$^{207}Pb/^{206}Pb$	±	$^{208}Pb/^{232}Th$	±	$^{206}Pb/^{238}U$	±
1,1	180	68	0,38	0,5	-	<0.01	309,88	9,82	0,0450	0,0091	0,00323	0,00011	20,81	0,70
2,1	3025	2977	0,98	8,2	-	0,34	317,88	3,99	0,0491	0,0016	0,00314	0,00004	20,18	0,26
3,1	2051	998	0,49	5,6	-	0,13	314,84	4,27	0,0475	0,0019	0,00317	0,00004	20,42	0,28
4,1	358	128	0,36	1,0	-	0,27	312,65	7,40	0,0485	0,0067	0,00319	0,00008	20,53	0,52
5,1	182	54	0,30	2,5	-	0,50	61,43	1,10	0,0520	0,0029	0,01620	0,00030	103,59	1,88
6,1	1326	635	0,48	3,6	0,001794	0,11	317,41	4,81	0,0473	0,0024	0,00315	0,00005	20,25	0,31
7,1	2070	591	0,29	5,6	0,000563	0,45	317,06	4,30	0,0500	0,0019	0,00314	0,00004	20,21	0,28
8,1	1313	596	0,45	3,6	-	0,11	310,12	4,71	0,0473	0,0023	0,00322	0,00005	20,73	0,32
9,1	738	302	0,41	2,0	0,002040	0,54	317,34	7,76	0,0507	0,0031	0,00313	0,00008	20,17	0,50
10,1	2740	4161	1,52	7,6	0,000312	0,47	309,26	3,98	0,0502	0,0017	0,00322	0,00004	20,71	0,27
11,1	3106	956	0,31	8,7	0,000321	0,44	308,21	5,78	0,0499	0,0016	0,00323	0,00006	20,79	0,39
12,1	2765	886	0,32	7,7	-	0,13	307,47	4,05	0,0475	0,0016	0,00325	0,00004	20,90	0,28
13,1	1297	731	0,56	3,7	0,001382	2,04	304,18	4,62	0,0626	0,0027	0,00322	0,00005	20,73	0,32
14,1	224	109	0,48	0,6	0,002989	0,59	308,13	9,79	0,0511	0,0111	0,00323	0,00011	20,77	0,72
15,1	2336	561	0,24	6,5	0,000244	0,43	308,28	4,05	0,0498	0,0019	0,00323	0,00004	20,79	0,28
16,1	1378	618	0,45	3,8	0,000913	0,32	311,96	4,73	0,0489	0,0024	0,00320	0,00005	20,57	0,32
17,1	1354	631	0,47	3,8	0,000619	<0.01	305,13	4,84	0,0453	0,0023	0,00328	0,00005	21,12	0,34
18,1	2186	1100	0,50	6,0	-	0,07	311,23	7,03	0,0470	0,0018	0,00321	0,00007	20,67	0,47
19,1	562	360	0,64	1,5	0,001989	0,36	317,02	6,78	0,0492	0,0036	0,00314	0,00007	20,23	0,44
20,1	631	240	0,38	1,7	0,001285	1,05	313,83	6,04	0,0547	0,0036	0,00315	0,00006	20,29	0,40
21,1	750	234	0,31	2,0	-	0,34	323,78	6,22	0,0491	0,0032	0,00308	0,00006	19,81	0,39
22,1	334	431	1,29	0,9	-	2,61	325,15	8,71	0,0671	0,0056	0,00300	0,00008	19,28	0,53

Notes:

1. Uncertainties given at the one σ level.
2. Error in Temora 1 reference zircon calibration was 0.45% for the analytical session. (not included in above errors but required when comparing data from different mounts.)
3. f_{206} [%] denotes the percentage of ^{206}Pb that is common Pb.
4. Correction for common Pb for the U/Pb data has been made using the measured $^{238}U/^{206}Pb$ and $^{207}Pb/^{206}Pb$ ratios following Tera and Wasserburg (1972) as outlined in Williams (1998).

Table 3: Isotopic geochemistry of the Packsaddle Volcanic Complex. clast (FC2362-A).

Sample	Rock type	Sm [ppm]	Nd [ppm]	$^{147}Sm/^{144}Nd$	$^{143}Nd/^{144}Nd$	$(^{143}Nd/^{144}Nd)_i$ (t=20 Ma)*	εNd	Rb [ppm]	Sr [ppm]	Rb/Sr	$^{87}Rb/^{86}Sr$	$^{87}Sr/^{86}Sr$	$(^{87}Sr/^{86}Sr)_i$ (t=20 Ma)*
Packsaddle Island													
FC2360	Ol-basalt	4,81	26,7	0,108918	0,512884	0,512870	5,0	21	923	0,02275	0,06580	0,70394	0,70392
11TU-5801	Basalt	4,78	26,1	0,110727	0,512893	0,512878	5,2	18	873	0,02062	0,05963	0,70389	0,70387
FC2362-A	Dacite clast	2,55	15,3	0,100763	0,512762	0,512749	2,7	82	570	0,14386	0,41608	0,70408	0,70396
Pacha Island													
FC2330	Dacite	1,86	10,7	0,105096	0,512812	0,512798	3,6	51	598	0,08528	0,24667	0,70453	0,70446
Hardy peninsula													
FC2349	Micro-gabbro	2,13	8,9	0,145512	0,512870	0,512851	4,7	6	393	0,01527	0,04415	0,70371	0,70369

Note:

*The initial ratios were calculated using the zircon age of ~20 Ma from the dacite tuff.